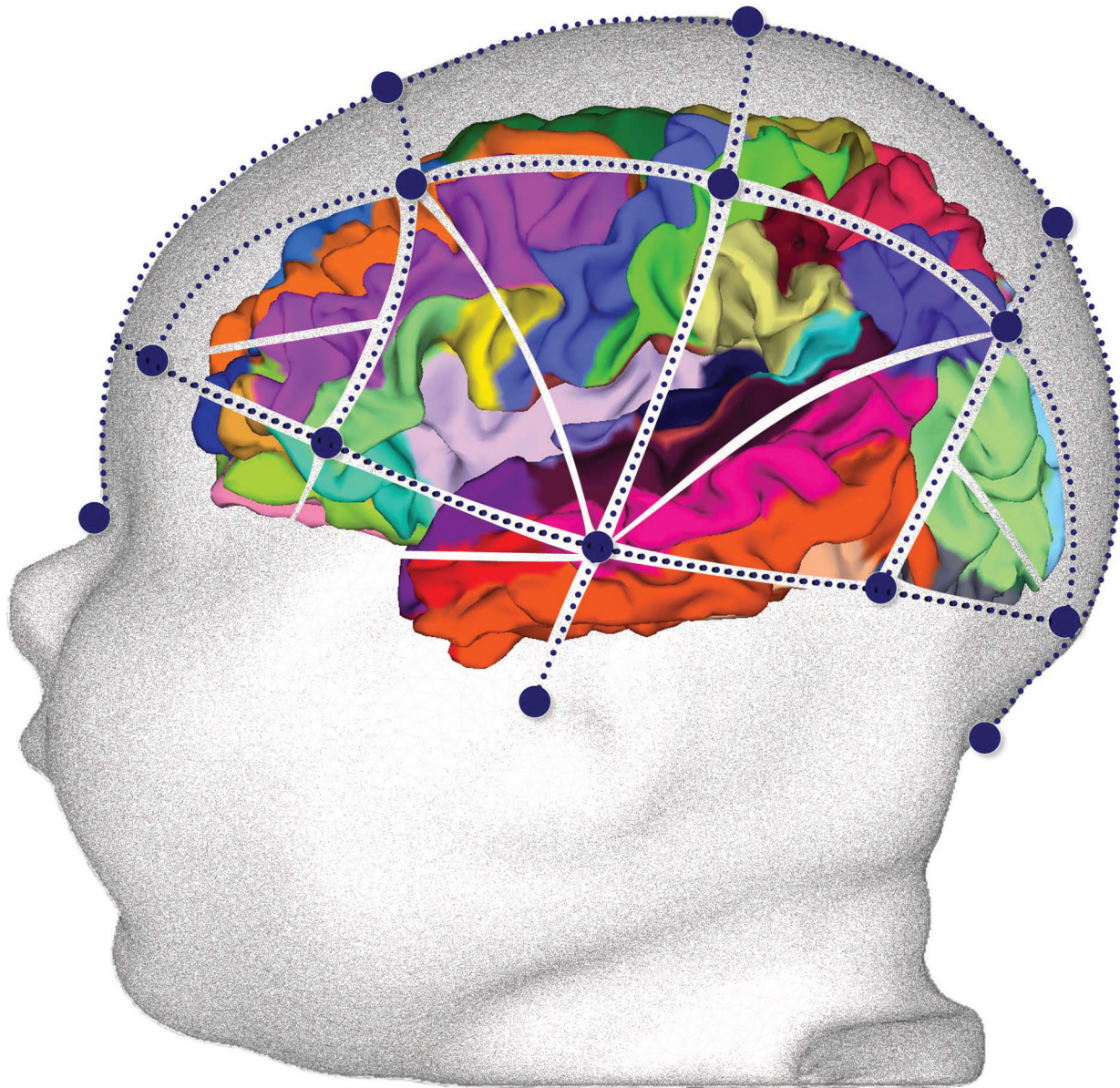


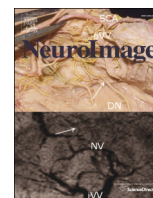
NeuroImage

Editor-in-Chief
Peter Bandettini



Available online at www.sciencedirect.com

ScienceDirect



Anatomical correlations of the international 10–20 sensor placement system in infants



C. Kabdebon^{a,b,c}, F. Leroy^{a,b,c}, H. Simmonet^{a,b,c}, M. Perrot^b, J. Dubois^{a,b,c}, G. Dehaene-Lambertz^{a,b,c,*}

^a INSERM, U992, Cognitive Neuroimaging Unit, F-91191 Gif/Yvette, France

^b CEA, DSV/I2BM, NeuroSpin Center, F-91191 Gif/Yvette, France

^c University Paris-Sud, Cognitive Neuroimaging Unit, F-91191 Gif/Yvette, France

ARTICLE INFO

Article history:

Accepted 15 May 2014

Available online 23 May 2014

Keywords:

Brain
Cognition
Development
NIRS
EEG
Source modelling

ABSTRACT

Developmental research, as well as paediatric clinical activity crucially depends on non-invasive and painless brain recording techniques, such as electroencephalography (EEG), and near infrared spectroscopy (NIRS). However, both of these techniques measure cortical activity from the scalp without precise knowledge of the recorded cerebral structures. An accurate and reliable mapping between external anatomical landmarks and internal cerebral structures is therefore fundamental to localise brain sources in a non-invasive way. Here, using MRI, we examined the relations between the 10–20 sensor placement system and cerebral structures in 16 infants (3–17 weeks post-term). We provided an infant template parcelled in 94 regions on which we reported the variability of sensors locations, concurrently with the anatomical variability of six main cortical sulci (superior and inferior frontal sulcus, central sulcus, sylvian fissure, superior temporal sulcus, and intraparietal sulcus) and of the distances between the sensors and important cortical landmarks across these infants. The main difference between infants and adults was observed for the channels O1–O2, T5–T6, which projected over lower structures than in adults. We did not find any asymmetry in the distances between the scalp and the brain envelope. However, because of the Yakovlevian torque pushing dorsally and frontally the right sylvian fissure, P3–P4 were not at the same distance from the posterior end of this structure. This study should help to refine hypotheses on functional cognitive development by providing an accurate description of the localization of standardised channels relative to infants' brain structures. Template and atlas are publicly available on our Web site (<http://www.unicog.org/pm/pmwiki.php/Site/InfantTemplate>).

© 2014 Elsevier Inc. All rights reserved.

The recent development of non-invasive brain imaging techniques has boosted research in cognitive development. Electroencephalography (EEG) and near-infra-red spectroscopy (NIRS) are particularly convenient when it comes to neonatal/paediatric brain recordings. Both of these techniques rely on an external placement of the recording sensors; an accurate description of the relations between the external anatomical landmarks and the internal cortical structures is therefore of crucial importance to draw robust interpretations from the recorded activity. It is not only true for NIRS, which records cortical activity in the crescent of light between a laser emitter and photodiode detectors; but also for EEG as responses might be more focal in infants than in adults due to the higher medium conductivity at this age (Grieve et al., 2003, 2004; Odabaee et al., 2013). Thus, an insufficient coverage of the head or a misplacement of the sensors relative to the cerebral structures of interest can lead to erroneous conclusions.

The international 10–20 system for electrode placement was originally developed to place EEG electrodes on the scalp in a reproducible manner from one recording to the next (Jasper, 1958). This standardised electrode positioning system is based on external landmarks, and a regular spacing between electrodes. It assumes a consistent relationship between scalp locations and underlying cerebral structures. The validity of this assumption has been demonstrated in adults (Homan et al., 1987; Jasper, 1958; Okamoto et al., 2004). However, very few studies have been conducted to tackle this issue during brain development, with only one post-mortem study in 6 infants, younger than 4 months of age (Blume et al., 1974), and a skull X-ray study in 28 infants between one week and thirteen months of age (Hellstöm et al., 1963).

This last study, which demonstrated a fixed location of the 10–20 system relative to fontanella and sutures, relied on the hypothesis that brain structures were also aligned to these skull markers. Yet, the inhomogeneous growth of the different cerebral lobes (Gilmore et al., 2007), the increase of the slope of the sylvian fissure during childhood (Sowell et al., 2002) and the operculation of the inferior frontal region observed during the first post-natal year are some examples of developmental changes that may affect the relations between brain structures and the 10–20 standardised scalp locations. Furthermore, the head shape

* Corresponding author at: Laboratoire de Neuroimagerie Cognitive INSERM U992, CEA/SAC/DSV/DRM/NeuroSpin, Bat 145, point courrier 156, F-91191 Gif/Yvette, France. Fax: +33 1 69 08 79 73.

E-mail address: gghislaine.dehaene@cea.fr (G. Dehaene-Lambertz).

may vary more during the first months of life than later on due to birth events and sleeping habits that may flatten one side of the head. Two potential sources of inter-subject variability may thus overlap: the external variability of sensor positioning and the internal structural variability.

In this study, we provided a broad description of the cranio-cerebral relationships of the 10–20 standard positions during the first 4 post-natal months, a time of fast developmental changes (i.e. brain volume doubles between birth and 6 months of age), with two distinct approaches to quantify both external and internal variability. We used MRI data, which give access to both external landmarks and cerebral organisation, in a cohort of 16 healthy infants. We worked on 3-D reconstruction of the infant's heads and brains using specific algorithms developed in the BrainVisa software (Cointepas et al., 2001) allowing realistic computations and visualisation of the relations between external and internal landmarks.

We first virtually placed electrodes over infant heads following the standardised 10–20 placement rules. Second, we choose one infant as representative of the group and projected on her the location of the individual electrodes localization after having normalised each infant anatomical image towards this template. Third, we specifically labelled 94 cortical regions (47 on each hemisphere) in our template infant adapting the MNI-space anatomical parcellation proposed for the adult brain by Tzourio-Mazoyer et al. (2002). We were thus able to analyse the electrode placement variability relative to the underlying cortical regions. Fourth, we examined the brain structural variability across our group and computed the main sulcal patterns distribution, to analyse cortical structures variability with respect to the 10–20 system. Finally, we reported electrode-brain distances since NIRS/EEG measurements are particularly sensitive to the depth of the cortical surface from the head scalp. Our description should provide an accurate view of the variability of standardised electrode locations over the scalp, and of their relationship with underlying cerebral structures in infants. It also provides the community with an anatomically defined infant atlas in order to study and describe cortical activity.

Materials and methods

Subjects

Sixteen healthy full-term infants (mean maturational age, that is, chronological age corrected for the gestational age at birth: 9.0 ± 3.6 weeks, range: 3.4–16.3 weeks; 11 boys, 5 girls) were included in this study after their parents gave written informed consent.

Data acquisition

Infants were naturally asleep during MR imaging (no sedation was used). Particular care was taken to minimise noise exposure, by using customised headphones and by covering the magnet bore with special noise protection foam. The study was approved by the regional ethical committee for biomedical research.

T1 and T2 weighted images covering the whole brain were acquired on a 3 T MRI system (Tim Trio, Siemens Medical Systems, Erlangen, Germany) using a 32-channels head coil. To minimise specific absorption rate (SAR) and noise exposure, we used radio-frequency (RF) impulses with “no SAR”, and the “whisper” gradients mode. The total acquisition time was 5 min 32 s (T1w = 2 min 48 s; T2w = 2 min 44 s). T1w images were obtained with a 3-D fast gradient recovery sequence (MPRage, TE/TR/TI = 4.25/1100/2000 ms, parallel imaging GRAPPA reduction factor 2, partial Fourier sampling factor 6/8). Sagittal slices were acquired with a spatial resolution of 1 mm isotropic (field of view = 192 mm; acquisition matrix = 192×192 , no interpolation at reconstruction; slice thickness = 1.1 mm; 176 slices). T2w images were obtained with a 2D turbo spin echo sequence (TSE, TE/TR = 149/4500 ms, 4 concatenations, parallel imaging GRAPPA reduction factor 2). Axial slices were

acquired with a spatial resolution of 1 mm isotropic (field of view = 192 mm; acquisition matrix = 192×192 , no interpolation at reconstruction; slice thickness = 1.1 mm; 92 slices).

T1w versus T2w images

In this study, we distinguished the variability for sensor placement over the skull from the variability of inner cerebral structures. At this age, the contrast between white and grey matter is weak in T1w images, and T2w images are preferred to analyse brain structures (Barkovich, 2000). By contrast, T1w images provide better information about the head shape, with a good contrast for the fat of the skin. We thus used T1w images to extract head shape and study sensor placement over the head, and T2w images to examine cortical organisation. T1w images and T2w images were registered to each other in each infant using linear transformation and depending on the analysis, we used one or the other sequence.

Template and atlas definition

Amongst our infants, we chose a 7.1 week-old girl as a template, because her age was close to the population's mean age and her head was regular and symmetrical. We also checked that the head was symmetrically positioned in the head coil to avoid that cerebral spinal fluid (CSF) settles on one side. We choose to adapt the Automated Anatomical Labeling (AAL) atlas (Tzourio-Mazoyer et al., 2002) to the infant's brain. We choose this atlas because, on the one hand, it provides a standardised anatomical labelling that is widely used notably in different softwares (e.g. SPM and Brainstorm), and on the other hand, it relies on identification of primary and secondary sulci, which are already clearly visible in the newborn's brain. Instead of manually drawing sulci landmarks on axial slices as it was done for this template (Tzourio-Mazoyer et al., 2002), we benefited from the 3-D reconstruction of the grey–white matter interface and of the automatic recognition of the sulci through the BrainVisa pipeline (Cointepas et al., 2001) to semi-automatically draw the ROIs on the brain surface.

Specifically, we performed the following steps. The first and most difficult step in infant is to obtain a correct reconstruction of the grey–white matter interface. The inner cortical surface was segmented using a semi-automatic segmentation pipeline dedicated to T2w MRI images of the infant brain (validation of this pipeline can be checked in Leroy et al., 2011b), followed by manual correction, when local inaccuracies were detected. In the fast maturing regions, such as the primary cortices, the T2w signal becomes darker with a blurring of the grey–white matter interface. This leads to segmentation inaccuracies particularly in these regions (Leroy et al., 2011b). The human eye being more accurate to follow the cortical ribbon, authors H.S. and F.L. systematically performed a visual inspection of the automatic segmentation along the central sulcus and the medial occipital regions. The 3-D reconstruction of the inner cortical surface was also checked looking for spiky regions, which are created when the grey–white matter interface is inaccurately drawn. Using Anatomist software (Riviere et al., 2000), the segmented white matter mask was projected over the axial MRI slices and author H.S. manually redrew the white matter mask using a one voxel paintbrush in every axial slice when inaccuracies were detected. Corrections were reviewed with F.L. to obtain the better consensus.

The anatomical parcellation was then performed on this corrected 3-D reconstruction of the inner cortical surface (Fig. 1). Through the BrainVisa pipeline (Cointepas et al., 2001), primary and secondary sulci were automatically extracted and labelled (Fig. 1). This step does not raise specific concern in infants compared to adults. Infants' sulci are generally simpler than adults' due to the fact that the tertiary gyration is just starting at this age. The sulci were visually checked by C.K. and relabelled when necessary, directly on the 3-D ribbon-like representations of the sulcal patterns – using Anatomist (Riviere et al., 2000). Corrections were systematically reviewed with F.L., and in difficult

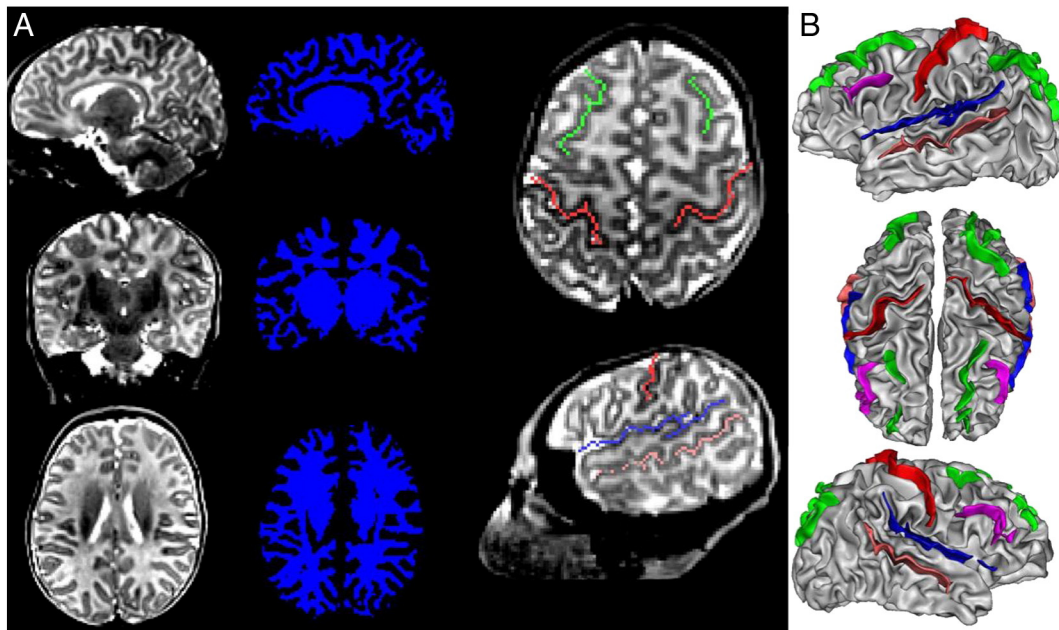


Fig. 1. Cortical segmentation and sulci extraction. A – White matter mask in blue, segmented using a semi-automatic segmentation pipeline (Leroy et al., 2011b) presented near the corresponding T2w slices of the 7.1-week-old template. B – A subset of the sulci computed using a dedicated BrainVisa algorithm (Cointepas et al., 2001) projected over the template T2w MRI slices and on its 3-D mesh. The same procedure was applied to all infants.

cases, with G.D.L. (neuropaediatrician) and L.H.P. (neuroradiologist and neuropaediatrician) until a consensus was reached (see Fig. 1 to appreciate the result).

On the basis of the segmented sulci, we delineated 47 anatomical regions of interest (ROIs), in each hemisphere. As explained in Tzourio-Mazoyer et al. (2002), almost all ROIs were delineated by sulcus fundi. Thus author C.K. delineated the parcels on the 3-D reconstruction of the grey–white matter interface using Anatomist drawing tool dedicated to brain folding patterns (Le Troter et al., 2012). This tool automatically extracts the line of the sulcal fundi on the mesh of any cortical surface by following the optimal path between any two points by minimising the (negative) mean curvature. When necessary, T2 slices aligned on the 3-D mesh using the Anatomist software (Riviere et al., 2000) were also considered to resolve ambiguous situations. When specific distances to a given structure were used to define a brain region in the adult's atlas (e.g. supplementary motor area), a 1.4 ratio was used to decrease this distance according to the size ratio between the adult and infant brains (Dehaene-Lambertz et al., 2002). Each region was reviewed (authors F.L., C.K. and G.D.L.), and in difficult cases, a consensus was obtained.

For practical reasons, two anatomical regions (pallidum and hippocampus) amongst the 45 defined in Tzourio-Mazoyer et al. (2002) were not included in our parcellation, because T2w images contrast and resolution were too poor at these locations. We could also not delineate a region labelled “inferior parietal cortex” in the right hemisphere of our template infant. It was defined by Tzourio-Mazoyer et al. (2002) as the remaining part of the inferior parietal lobule that was not belonging to the supramarginal nor to the angular gyrus. This observation was subject specific, and should not be considered as a general fact about infant neuroanatomy. We brought some additional refinements to the AAL atlas (Tzourio-Mazoyer et al., 2002), as the temporal region lining the inferior plane of the sylvian fissure cannot be considered as homogeneous. First, we labelled Heschl's gyrus, being the most anterior gyrus on the upper surface of the temporal lobe. This gyrus is bordered posteriorly by the Heschl's sulcus. The *planum temporale* was then defined as the triangular structure lying on the upper surface of the temporal lobe, inside the sylvian fissure, limited anteriorly by Heschl's sulcus. We defined the posterior limit of the *planum temporale* at the last coronal section before a change in the slope of the continuous plane characterising the *planum temporale*. Any posterior territory was

labelled as *planum parietale*. The region on the floor of the sylvian fissure anterior to the Heschl's gyrus, and posterior to the superior temporal pole (defined in Tzourio-Mazoyer et al., 2002) was labelled as *planum polare*.

The proposed parcellation (Fig. 4) is a single-subject atlas as several atlases proposed in adults (Talairach and Tournoux, 1988; Tzourio-Mazoyer et al., 2002), and is therefore specific to our template (i.e. a 7.1 week-old infant) but as it keeps the adequate resolution of a single subject, it can be used as a template for source reconstruction, as proposed in Brainstorm (Tadel et al., 2011) for example.

External 10–20 sensors placement

The international 10–20 standard positions were virtually set on each individual infant head reconstruction using a semi-automated algorithm (Fig. 2-A). The infants' head volumes were first extracted from the T1w MRI images, and reconstructed in 3-D. Then, the four standard fiducial positions (nasion, inion, left and right tragi) were located by C.K. over the head 3-D reconstruction, with the help of T1w MRI volumes, based upon anatomical considerations. First, the nasion was defined as the distinctly depressed area directly between the eyes, just superior to the bridge of the nose. The inion was the lowest point of the skull from the back of the head, and we systematically located this point on the inferior side of the external occipital protuberance. Regarding the left and right pre-auricular points, originally used for the lateral measurement in the 10–20 system, we choose to replace them with the upper limits of the left and right tragi, as it is actually often the case in clinical situations, due to difficulty in their detection. It has been shown that this subtle difference in pre-auricular point definition has a very limited impact on the 10–20 standard positions (Jurcak et al., 2007). As a result, for each ear, the tragus was defined as the upper point of the small pointed eminence of the external ear.

The four fiducial positions were then used to generate a system of geodesic lines that run along the 3-D head shape and intersect at intervals of 10% and 20% of their total length following the standardised 10–20 description (Fig. 2-B). An iterative algorithm following these definition rules was designed to automatically locate the 19 sensors in each infant: The geodesic distance maps were computed from the landmarks over the skull, using BrainVisa image processing tools (Cointepas et al., 2001). We defined two sets of points with these distance maps: those

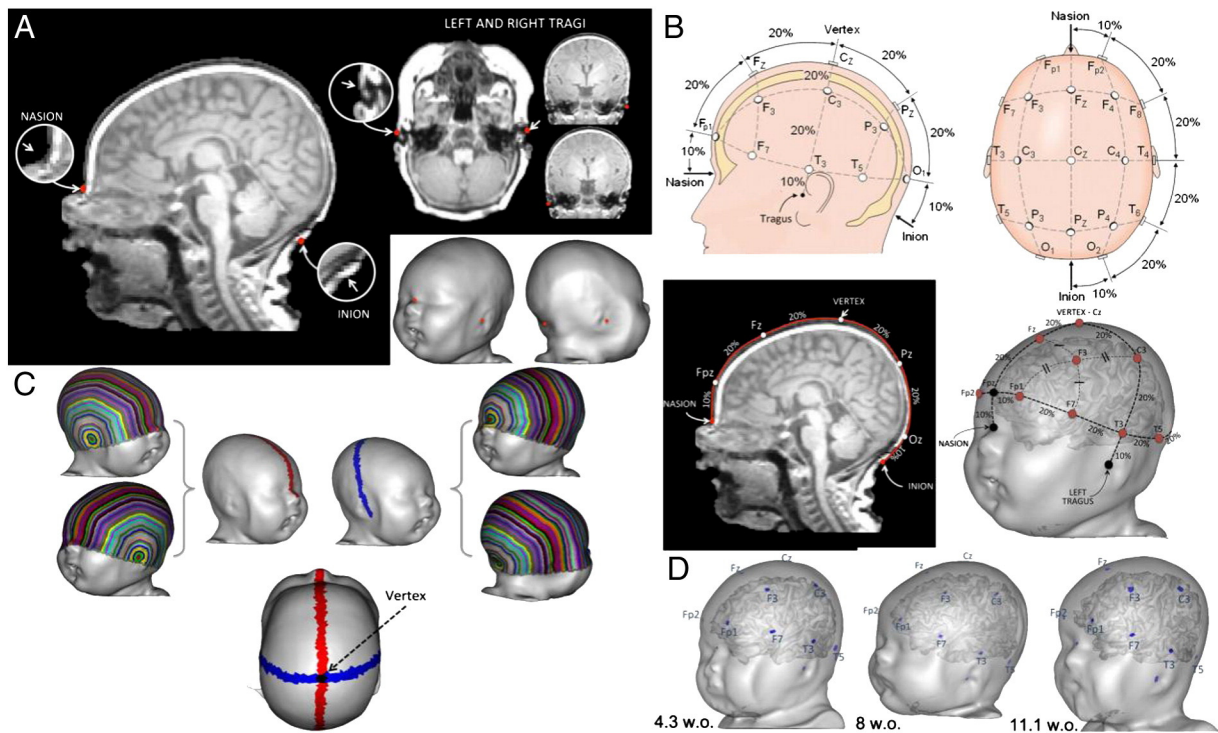


Fig. 2. The international 10–20 system for electrode placement. A – The four anatomical reference points are presented on the 7.1-week-old infant, selected to be the template. B – The international 10–20 standard cranial positions as defined in Jasper (Jasper, 1958) and reported on the template. C – An algorithm based on geodesic distance maps was used to automatically define electrode positions. Here is shown how the vertex was defined on the template. D – Example of electrodes automated localization on three different subjects of different ages (4.3-week-old on the left, 8-week-old on the centre, 11.1-week-old on the right).

equidistant from the left and right tragi, and those equidistant from the nasion and the inion. The vertex was then computed as the intersection of these two sets of points (Fig. 2-C). The line joining the nasion and the inion through the vertex was computed as the intersection of the plane defined by these 3 points and the baby's skull. A geodesic distance map was computed along this line, and we set the frontal sensor Fz and the parietal sensor Pz along the geodesic line at 30% and 70% of the total distance, from the nasion, respectively; additionally the midline points Fpz and Oz were located at 10% and 90% of the total distance. Similarly, the line joining the two tragi through the vertex was computed as the intersection of the plane defined by these 3 points and the baby's skull, and the four points T3, T4, C3, C4 were set along the left-right tragi geodesic line (at respectively 10%, 90%, 30% and 70% of the total length). Again, the line joining the midline points Fpz and Oz through T3 was computed as the intersection of the plane defined by these 3 points and the baby's skull, and the four transversal points Fp1, F7, T5 and O1 were located along this line on the left side (at 10%, 30%, 70% and 90% of the entire distance away from Fpz); and the same procedure was conducted on the right side to mark Fp2, F8, T6 and O2. Eventually, we defined the four points F3, F4, P3 and P4 along geodesic lines at the equidistant locations from the neighbouring sensors. The sensor locations were then stored as a binary mask for each infant, that is a volume with one voxel per sensor location set to 1, and the other voxels set to 0.

Brain structures segmentation

In order to investigate the variability of the inner brain structures at the population level, we identified some relevant cortical landmarks over the infant group, and modelled the sulcal presence probability and inter-subject variability. Because of both sulcal variability and potential local inaccuracies in cortical segmentation of the most mature and twisted parts of the brain (e.g. the calcarine sulci), we restricted our set of sulci to the most reliable ones, namely, the lateral sylvian fissure (SF), the central sulcus (CS), the superior temporal sulcus (STS) and

its ascending branch, the superior frontal sulcus (SFS), the inferior frontal sulcus (IFS) and its anterior part, and the intraparietal sulcus (IPS). The sulcal patterns extraction algorithm crucially depends on the quality of the MRI images, and it failed for one infant, who was thus removed from this analysis. For each infant, skull stripping and the extraction of the inner cortical surface were performed using the same automatic segmentation pipeline, dedicated to T2w MRI images of the infant brain, than for the template. For all infants, a neuropaediatrician (H.S.) visually checked and manually corrected the segmentation result when local inaccuracies occurred, and each segmented brain was thereafter reviewed (H.S. and F.L.). We obtained the interface between cortex and white matter for each hemisphere, saved as binary images, as well as 3-D reconstructions.

We identified sulci through a BrainVisa pipeline (Cointepas et al., 2001), providing a first automatic extraction and labelling, from the grey–white interface reconstruction. A manual checking and relabelling were performed when necessary by two of the authors (C.K. and F.L.). For difficult cases (small or segmented sulci might be ambiguous), a consensus was obtained with LHP and GDL. The manual labelling was performed directly on the 3-D meshes – 3-D ribbon-like representations of the sulcal patterns – using Anatomist.

Normalisation

For each subject, we non-linearly normalised the individual T1w (or T2w) image onto the single-subject template T1w (or T2w) using the Statistical Parametric Mapping toolbox in matlab (SPM8), and visually checked the match of each individual image to the template. Due to the specific characteristics of T1w and T2w at this age, T1w images were preferred to align the skull shapes for the measures of inter-subject sensors variability, whereas T2w images are better to align cortical structures. Both images being linearly aligned within each subject using spm8, the relation between external landmarks and brain structures was maintained.

Inter-subject sensors variability

We applied the T1w normalisation matrix to the sensor binary images, using the nearest neighbour interpolation in each infant. Then the registered binary masks were averaged over the template head and smoothed using a small Gaussian filter (filter size: 1.1 mm, isotropic). It produced an “average” sensor net made of 19 regular regions – one for each sensor.

For a more accurate description of the sensors' locations with respect to the underlying brain structures, we projected the set of the registered sensors onto the template brain envelope. For the projection, we defined sensors as spheres centred on the standard locations, with a 5 mm diameter. The brain envelope is a smooth surface overlapping the crown of gyri, where folded patterns are removed. It was computed

from the binary images of the grey–white matter interface: applying a morphological closing (structuring element size: 15 mm), followed by a morphological dilation (structuring element size: 2 mm). These envelope images were also reconstructed in 3-D. The projection of a given sensor was defined as the closest point of the brain envelope from the average sensor. A Gaussian smoothing (filter size: 2.2 mm, isotropic) was then applied to the projected set of average sensors to regularise the distribution estimate. Over the template brain envelope, we delineated two isosurfaces for each of the 19 sensors, one containing 90% of the population and the other 50% (Fig. 5-B). These isosurfaces were computed, for each electrode, by gradually integrating the distribution estimate from the highest likelihood down to the thresholds for which the isosurfaces include 50% and 90% of the infants' sensor projections,

Table 1
Labels and corresponding surfaces of the 47 anatomical regions of interest defined in each hemisphere of the template infant.

Region	Label	Left hemisphere		Right hemisphere		
		Surface (mm ²)	Percentage of hemispheric surface	Surface (mm ²)	Percentage of hemispheric surface	
Frontal	Lateral ventricle and remaining tissues	1	3904	9.72%	3402	8.38%
	Insula	2	1037	2.58%	1044	2.57%
	Lateral surface					
	Inferior frontal gyrus, opercular part	3	611	1.52%	499	1.23%
	Inferior frontal gyrus, triangular part	4	862	2.15%	812	2.00%
	Middle frontal gyrus	5	2137	5.32%	2631	6.48%
	Superior frontal gyrus	6	1468	3.66%	1469	3.62%
	Medial surface					
	Medial superior frontal gyrus	7	741	1.84%	918	2.26%
	Supplementary motor area	8	1407	3.50%	1265	3.11%
	Orbital surface					
	Olfactory bulb	9	217	0.54%	193	0.48%
	Gyrus rectus	10	321	0.80%	431	1.06%
	Orbitary frontal medial	11	333	0.83%	304	0.75%
Orbitary inferior frontal gyrus	12	673	1.68%	691	1.70%	
Orbitary middle frontal gyrus	13	502	1.25%	508	1.25%	
Orbitary superior frontal gyrus	14	519	1.29%	520	1.28%	
Central	Lateral surface					
	Rolandic operculum	15	617	1.54%	660	1.63%
	Precentral gyrus	16	1662	4.14%	1504	3.70%
	Postcentral gyrus	17	1383	3.45%	1450	3.57%
	Medial surface					
	Paracentral lobule	18	847	2.11%	1056	2.60%
	Parietal	Lateral surface				
Angular gyrus		19	1316	3.28%	1721	4.24%
Supramarginal gyrus		20	1192	2.97%	969	2.39%
Inferior parietal gyrus		21	449	1.12%		
Superior parietal gyrus		22	1238	3.08%	1317	3.24%
Medial surface						
Temporal	Precuneus	23	1190	2.96%	1629	4.01%
	Middle temporal pole	24	229	0.57%	454	1.12%
	Superior temporal pole	25	641	1.60%	717	1.77%
	Inferior temporal gyrus	26	2164	5.39%	1789	4.40%
	Middle temporal gyrus	27	1707	4.25%	1873	4.61%
	Superior temporal gyrus	28	833	2.08%	641	1.58%
	Heschl gyrus	29	453	1.13%	292	0.72%
	Planum parietale	30	288	0.72%	278	0.68%
	Planum temporale	31	223	0.56%	189	0.46%
	Planum polare	32	316	0.79%	270	0.66%
Occipital	Lateral surface					
	Inferior occipital gyrus	33	723	1.80%	1081	2.66%
	Middle occipital gyrus	34	1581	3.94%	2101	5.17%
	Superior occipital gyrus	35	471	1.17%	510	1.26%
	Medial surface					
	Fusiform gyrus	36	1143	2.85%	782	1.93%
	Lingual gyrus	37	494	1.23%	499	1.23%
Calcarine sulcus	38	703	1.75%	788	1.94%	
Limbic	Cuneus	39	863	2.15%	794	1.96%
	Parahippocampal gyrus	40	385	0.96%	339	0.84%
	Amygdala	41	84	0.21%	105	0.26%
	Posterior cingulate gyrus	42	353	0.88%	331	0.81%
	Middle cingulate gyrus	43	370	0.92%	338	0.83%
Nuclei	Anterior cingulate gyrus	44	704	1.75%	700	1.72%
	Putamen	45	60	0.15%	55	0.14%
	Caudate	46	179	0.45%	214	0.53%
	Thalamus	47	560	1.39%	481	1.18%

respectively. We additionally computed the standard deviation of the spatial distribution for each sensor along the three directions (Table 2).

Inter-subject sulcal mapping

To examine the localization and variability of the inner cerebral structures, we built an atlas of sulcal patterns at the population level, modelling sulcal presence probability across infants. For each sulcus label, we built frequency maps, in which each voxel stores the number of subjects whose sulcus was identified at this location. We applied the T2w normalisation matrix to the sulcal binary images, using the nearest neighbour interpolation in each infant to project each map in our reference template. To reduce the dispersion of individual sulcus location due to our small population size (15 infants), we performed an isotropic Gaussian smoothing (filter size: 1.7 mm, isotropic) on each sulcus. We then estimated the spatial probability of finding a sulcus in a given voxel by dividing each voxel by a normalisation factor: the sum of all the voxels of the 3-D space. This normalisation ensures that the probability integrates to 1 over the spatial 3-D space. We obtained sulcal SPAM (Statistical Probabilistic Anatomy Map) (Evans et al., 1994; Perrot et al., 2011). We thereafter represented the sulcal models as volumes, using an isosurface corresponding to 60% of the whole probability mass, computed by integrating the probability from the highest likelihoods to the lowest (Fig. 7-B).

The isosurface provides localisation information about the structures. However, this 3-D representation comes with a main drawback: it mixes information about the size of the sulcus and the inter-subject variability. In other words, a large 3-D sulcal model might either mean a large sulcus or a variable structure across subjects. To overcome this ambiguity, we defined dispersion as a “density” measurement along each sulcus, defined from the smoothed sulcal frequency maps. For each section along the considered sulcus, we defined dispersion as the ratio of the sum of voxels in the sulcal model, to the sum of true sulcal voxels in the same section.

Depth measurements

We first generated a mean depth map over the skull of the template subject (Beauchamp et al., 2011; Okamoto et al., 2004), showing the distance distribution from the brain envelope surface to the skull, averaged over the 16 infants: For each infant, we computed, on non-normalised brains, the brain-scalp distance at each point of the head, using distance maps, and we saved this depth information as a volume. We thereafter registered the computed depth volumes to the template space using the non-linear transformations computed on the T1w images.

We secondly investigated sensor-brain distances. To address this question, we considered two different approaches to extract distances on the raw images. First, we performed, for each infant, a basic computation of the distance between each sensor on the scalp and the closest point of the brain tissue, defined on the brain envelope from the sensor. However, experimenter might be more interested by the distance between the sensors and some remarkable cerebral structures. Thus, we manually defined four cortical landmarks in each of the 16 infants (Fig. 3) with the help of the T2w images and the grey-white interface reconstructions. We identified the most posterior point of the hand knob, in the depth of the central sulcus, the ventro-lateral tip of the pars triangularis, below the triangular sulcus, the lateral edge of Heschl's sulcus, and the posterior end of the sylvian fissure, each landmark on the left and right hemispheres. The closest sensors, and their contralateral homologs were then identified for each cortical landmark, and the landmark-sensor euclidean distances were computed. Note here that the cortical landmarks were manually selected on the grey-white interface, not the envelope. We also measured in each infant the distances between tragi,inion-nasion and vertex-tragi line (Table 4).

Since structural asymmetries are particularly at stake in developmental studies, we thereafter examined whether landmark-sensor distances were similar on the left and right hemispheres. For each sensor left-right pair, we thus computed an asymmetry coefficient of the distance to ipsilateral landmark (D) defined as $(\text{Right} - \text{Left})/0.5 * (\text{Right} + \text{Left})$, and we tested whether the left (or right) distance was significantly larger

Table 2
Variability of the 10–20 international standard positions.

Electrode	Left-right Standard-deviation (mm)	Antero-posterior Standard-deviation (mm)	Dorso-ventral Standard-deviation (mm)	Standard-deviation (mm)
Frontal				4.02
Fp1	2.09	1.36	2.45	3.49
Fp2	2.17	1.70	2.55	3.76
Fz	2.47	2.25	1.90	3.84
F3	2.28	2.74	2.65	4.45
F4	2.25	2.77	2.22	4.20
F7	1.98	2.57	2.79	4.28
F8	1.81	2.32	2.91	4.14
Central				4.92
Cz	2.45	3.36	1.71	4.49
C3	2.28	3.21	3.23	5.09
C4	2.11	4.13	2.29	5.17
Temporal				5.26
T3	1.51	4.03	3.94	5.83
T4	1.32	2.83	3.78	4.90
T5	2.12	3.53	4.25	5.92
T6	1.54	2.64	3.11	4.37
Parietal				5.31
Pz	2.74	2.31	3.64	5.10
P3	2.44	2.47	4.40	5.60
P4	2.68	3.36	2.96	5.21
Occipital				5.13
O1	2.87	2.60	3.76	5.40
O2	3.16	2.03	3.08	4.86
L vs R t-test p value	0.52	0.75	0.03*	0.08

Once individual data have been normalised to the template, the standard deviation of the centre of the virtual electrode has been computed across the group along each of the 3-D coordinates (left-right, antero-posterior and dorso-ventral axes) and using the Euclidian distance (last column). The average variability (mean Euclidian distance across local channels) is also presented for the main areas (frontal, central, temporal, parietal and occipital). The last line presents a paired t-test comparing the 8 left and right locations for each measure ($df = 7$).

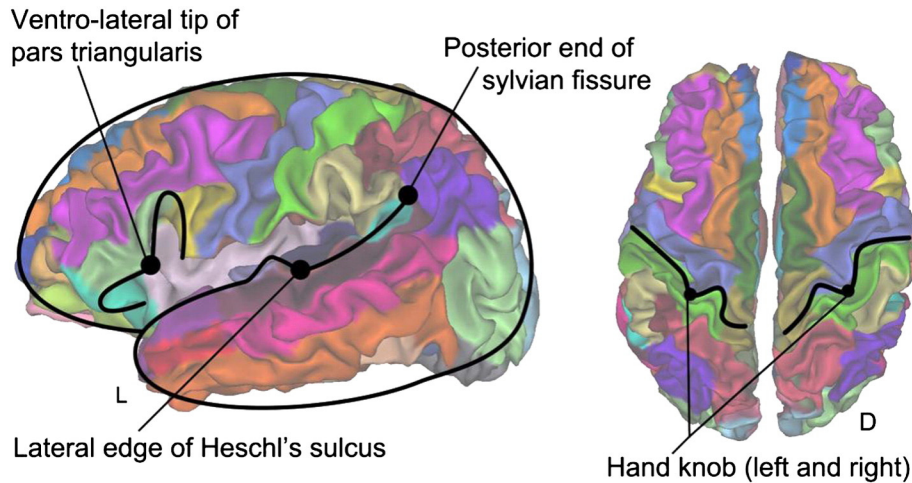


Fig. 3. Localisation of the cortical landmarks used for depth measurements on the template: posterior end of the lateral fissure, the ventro-lateral tip of the pars triangularis, the lateral edge of the Heschl's sulcus, and the most posterior point of the hand knob, in the depth of the central sulcus (left and dorsal views).

using a two-tailed paired *t*-test between left and right distances for each landmark. We additionally computed the distance between the tragus and the posterior end of sylvian fissure, and performed the same tests for asymmetry. These regions support asymmetric functions and it is important in brain imaging studies investigating these functions to ensure that the external sensors, in particular NIRS sensors, are not themselves located asymmetrically relative to these landmarks.

Results

Template atlas

The anatomical parcellation of the template brain is depicted in Fig. 4, with the corresponding labels detailed in Table 1. We additionally computed the surface areas of the 47 regions of interest in each hemisphere.

10–20 standard positions localisation and variability

The standard deviations of the spatial distributions of the 10–20 sensors over the scalp are presented in Table 2, based on the 16 infants

normalised to the template, and expressed in the template subject coordinate system. Fig. 5-A and B depict probability maps for sensor locations over the template head surface and the template brain envelope surface. Fp1 and Fp2 were the most stable sensors, with the smallest standard deviation. Temporal and parietal sensors showed a large scattering. Paired *t*-test on the variability in each direction on the left versus right channel locations showed a larger dorso-ventral variation on the left relative to the right hemisphere ($p = .027$; proportion of left hemisphere sensors distributions larger than their right counterparts = 75%). Thus, the scattering of channel locations tended to be larger on the left than on the right hemisphere.

Brain structures localisation and variability

We also examined the cerebral structure variability: Fig. 7-B displays the sulcal models for six main cortical sulci over the infant population, providing estimates of the presence probability for each sulcus. Note that in line with the literature (Glaser et al., 2011), the sylvian fissure and the superior temporal sulcus showed a posterior ascending branch on the right side, whilst they remained rather horizontal on the left side.

Table 3

Projections of the 10–20 standard positions onto the template's cerebral structures (listed in a rank order), and in *italic*, onto the probabilistic sulci maps (SPAM).

Electrode	Anatomical region	Electrode	Anatomical region
Fp1	Orbitary superior frontal gyrus Orbitary inferior frontal gyrus Middle frontal gyrus	Fp2	Orbitary superior frontal gyrus Orbitary inferior frontal gyrus Middle frontal gyrus
F3	Middle frontal gyrus	F4	Middle frontal gyrus
F7	Inferior frontal gyrus, triangular part Orbitary middle frontal gyrus <i>Anterior to IFS</i>	F8	Inferior frontal gyrus, triangular part Orbitary middle frontal gyrus <i>Anterior to IFS</i>
C3	Postcentral gyrus Supramarginal gyrus <i>Posterior to CS</i>	C4	Postcentral gyrus Supramarginal gyrus <i>Posterior to CS</i>
T3	Middle temporal gyrus Inferior temporal gyrus <i>Anterior portion of STS</i>	T4	Superior temporal sulcus Middle temporal gyrus <i>Anterior portion of STS</i>
T5	Inferior temporal gyrus, posterior part	T6	Inferior temporal gyrus, posterior part
P3	Angular gyrus	P4	Angular gyrus
O1	Middle occipital gyrus Middle occipital gyrus Inferior occipital gyrus	O2	Middle occipital gyrus Middle occipital gyrus Inferior occipital gyrus
Fz	Supplementary motor area Medial superior frontal gyrus	Cz	Paracentral lobule Supplementary motor area
Pz	Superior parietal gyrus Superior occipital gyrus		

Table 4
Head measures.

	Mean	Standard deviation
<i>Infant population</i>		
Left to right tragi (mm)	102.90	5.56
Nasion to inion (mm)	122.60	5.49
Tragi line to vertex (mm)	97.97	7.02
Mean cerebral envelope (cm ³)	481.61	68.46
Radius of the corresponding sphere (mm)	48.54	0.22
<i>Template</i>		
Left to right tragi (mm)	93.52	
Nasion to inion (mm)	117.77	
Tragi line to vertex (mm)	92.89	
Mean cerebral envelope (cm ³)	412.79	
Radius of the corresponding sphere (mm)	46.20	

Fig. 6 displays a measurement for dispersion over SPAM models: it indicates the degree of overlap between subjects' sulci. The intraparietal sulcus and frontal sulci exhibit strong variability, whilst the sylvian fissure and the superior temporal sulcus are rather stable sulci. Inter-subject variability is especially visible at the ends of the sulci, due to the differences in size.

Relations between scalp sensors and cerebral structures

The projection of the electrodes over cerebral structures is convergent across both approaches (electrode distribution projected on the template and template electrodes projected on sulcal probability maps) suggesting a stable relation between external landmarks and cerebral structures (Table 3). Fig. 7-A and Table 3 summarise the anatomical relationships between the international 10–20 standard positions and the underlying cortical structures. Sensors Fp1 and Fp2 projected

over the orbital part of the frontal lobe, F3 and F4 over the middle frontal gyrus, C3 and C4 over the postcentral gyrus, and T5 and T6 projected on the posterior part of the inferior temporal gyrus. F7 and F8 overlaid the inferior frontal gyrus, pars triangularis. Interestingly, anterior temporal sensors did not project exactly over the same structures on the left and right hemispheres: T3 being slightly more ventral (left middle/inferior temporal gyri) than T4 (right superior/middle temporal gyri). This asymmetry is less obvious when SPAMS were considered, both electrodes projecting on the ventral part of the superior temporal sulcus. Occipital sensors O1 and O2 were located above the inferior and middle occipital gyri, whilst parietal sensors P3 and P4 overlapped the angular gyrus and the middle occipital gyrus. The midline standard positions Fz, Cz, and Pz, were located on, or near, the inter-hemispheric fissure.

Depth measurements

For external recordings, the distance between the captors and the brain is of crucial importance. For each infant, we thus measured the distance between the skull and the brain envelope from all points on the head surface and created an averaged cortical surface depth map over the infant group. We observed an anterior-posterior gradient with occipital cortex being closer to the surface than frontal cortex (Fig. 8-A). The skull was also more distant from the cortical envelope along the midline due to the superior sagittal sinus running in the longitudinal fissure.

To quantify this description, we first measured the distance between the 10–20 standard positions on the head surface and their cortical projection over the brain envelope for each infant. We confirmed the anterior-posterior gradient for brain depth with smaller electrode-envelope distances for posterior electrodes, and larger distances for the most anterior positions. This gradient is not present in adults (Fig. 8-B,

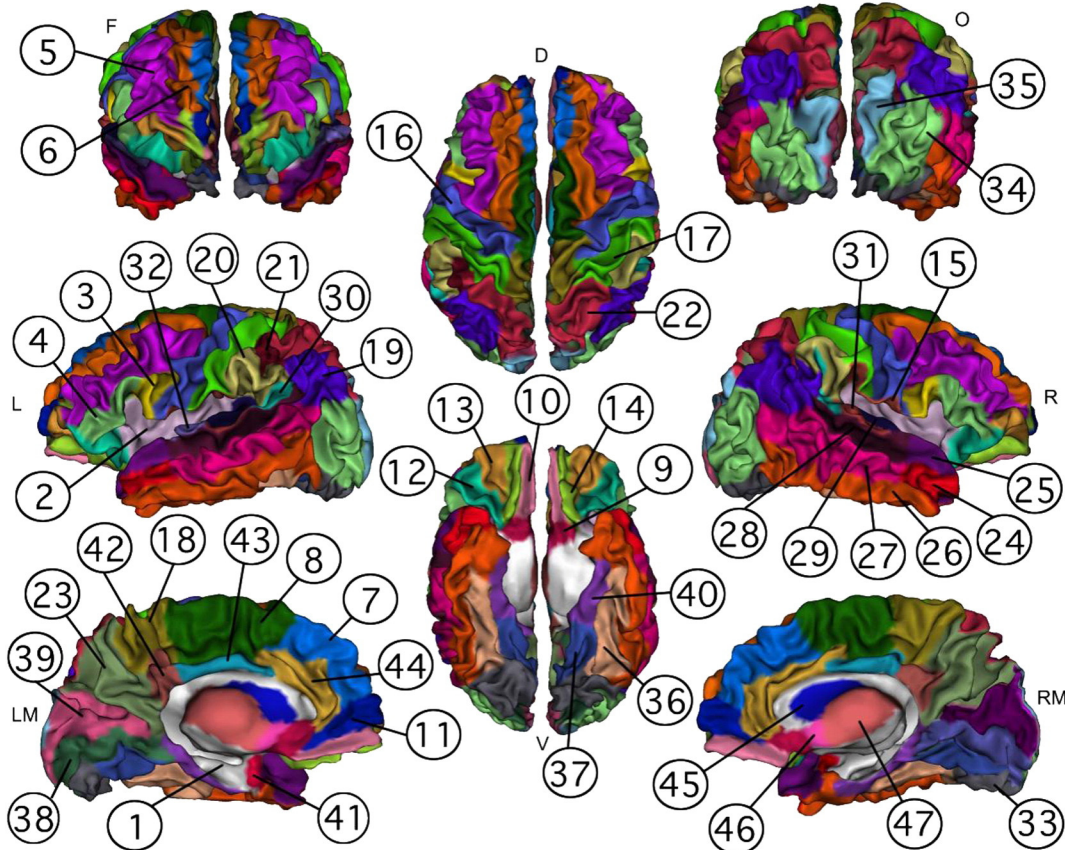


Fig. 4. Brain atlas. Different views of the anatomical parcellation of the template infant's brain (from top to down and left to right: Frontal – Left lateral – Left Medial; Dorsal – Ventral; Occipital – Right Lateral – Right Medial). See Table 1 for the parcel names.

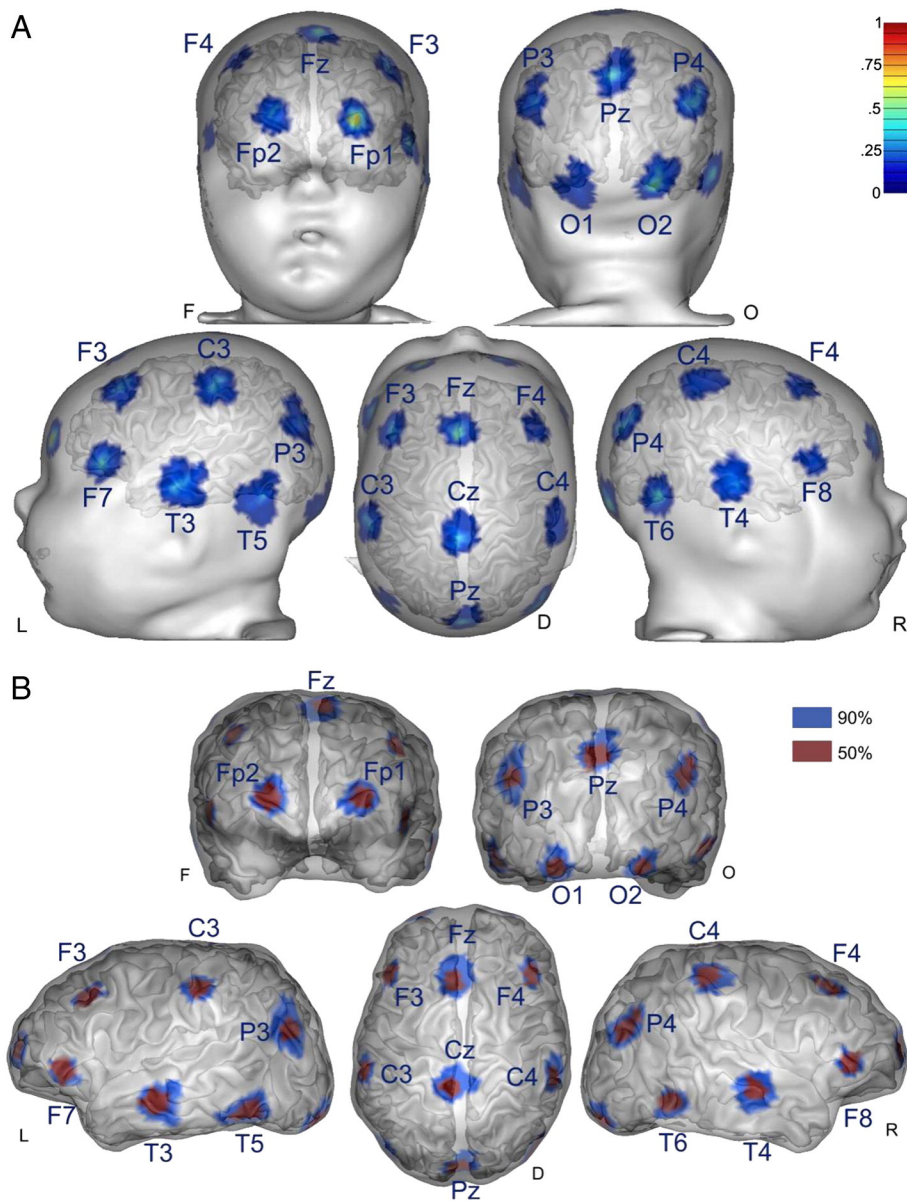


Fig. 5. 10–20 standard positions and their cortical projections. A – International 10–20 sensors' location distributions computed across the 16 infants, and showed over the skull of the template infant, with the underlying 3-D reconstruction of the grey-white matter interface (from left to right and top to down: Frontal – Occipital; Left – Dorsal – Right). B – International 10–20 standard positions distributions, projected on the brain envelope, with the underlying grey-white matter interface. Red surfaces encompass 50% of the subjects and blue surfaces 90% (from left to right and top to down: Frontal- Occipital; Left – Dorsal – Right views). FP1–FP2 are the most stable sensors.

data extracted from Okamoto et al., 2004). However, just as adults, the most distant electrodes from the brain are the midline positions (Cz, Fz, Pz). Both in the infant and adult groups, there are no difference between the left and right sides. Depth and asymmetry measurements are summarised in Table 5 and 4 provide generic head measures to report these distances to infant head size.

We additionally measured the distances between four precise cortical landmarks and the overlying 10–20 positions. For the hand knob, the ventro-lateral end of the pars triangularis, and the lateral edge of Heschl's sulcus, distances were similar in the right and left hemispheres, but the posterior end of the sylvian fissure was significantly closer to P3 and more distant from C3 on the left and thus tended to be closer to C4 and more distant from P4 on the right because of its different shape and slope in the left and right hemisphere. However, we found no asymmetry in distances between tragus and the posterior end of sylvian fissure, similarly to what Mahmoudzadeh et al. (2013) reported in preterms.

Discussion

Our goal was to provide the community of developmental cognitive researchers with an accurate description of the international 10–20 standard electrode locations relative to the underlying cerebral structures in infants, and an anatomical parcellation of a 2-month-old infant brain to localise the brain functional activity once data obtained by EEG or NIRS are registered to this template. As the brain is growing very fast after birth, we limited our age-range to the first four post-natal months (3–16 weeks). We investigated whether the relationships between external landmarks and brain structures were reliable during this developmental period when the head and the brain undergo quick growth (0.5 cm per week). We provided two complementary measures for cranio-cerebral relationships. With the first measure, we quantified the variability of the standard positions between infants, with respect to the underlying brain structures of the template infant. To complement this first approach,

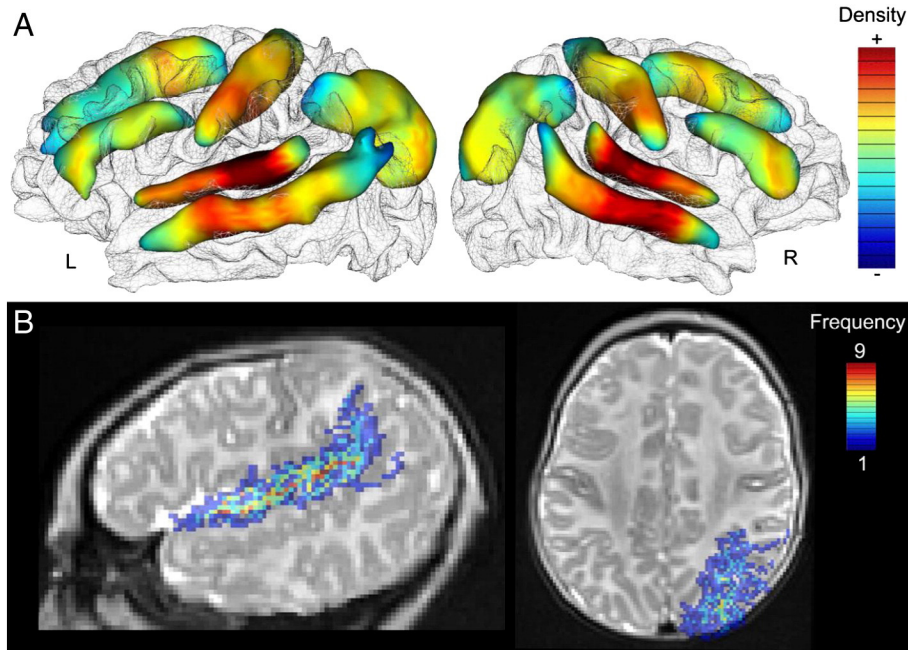


Fig. 6. Density values along sulci. A – Inter-subject structural variability modelled by a density measurement along the 60% isosurfaces of SPAM models (Left – Right), arbitrary units. A robust reproducibility across subjects is indicated by the red colour whereas the blue colour indicates a high variation across subjects. B – Two examples of inter-subject variability are presented over a sagittal and axial slice of the template MRI: The 15 normalised sulci show a higher degree of overlap for the sylvian fissure, on the left, compared to the intraparietal sulci, on the right.

the second measure focused on the localisation and variability of the internal cerebral structures over the group, with respect to the 10–20 theoretical standard positions of the template infant. We also provided additional information about brain-skull distances and their variability, and studied potential asymmetries of the distance between external sensors and cerebral landmarks.

The infant template

As template, we chose an infant with a symmetrical head (i.e. not distorted by birth or sleeping habit) and high quality T1w and T2w images, in the median of our age range. For the anatomical parcellation, we had no particular difficulties to follow the principles used by Tzourio et al. in adults, based on sulcal delineation confirming that the main macroscopical landmarks are well developed from birth on. We added the *planum temporale*, *planum parietale* and *planum polare* as they are important structures that were not reported in the Tzourio-Mazoyer et al.'s atlas (2002), because of a specificity of their template subject who had not the classical larger left *planum*. We did not parcel the pallidum and hippocampus, which are small and internal structures, difficult to segment in the infant brain.

As it is the case in the Tzourio-Mazoyer et al.'s (2002) and Talairach and Tournoux's (1988) atlases in adults, or more recently in Matsui et al.'s 12-month-old infant study (Matsui et al., 2014), our labelling relies on a single subject. As opposed to multi-subject-based probabilistic atlases (Akiyama et al., 2013; Altaye et al., 2008; Fonov et al., 2011; Kuklisova-Murgasova et al., 2011), single-subject atlases have a main drawback: the brain shape and anatomical structures might be biased by the subject's particularities. However, it has recently been reported (Tsuzuki and Dan, 2013) that, when it comes to functional group analyses, anatomic structural differences between single-subject and multi-subject based atlases are not substantial. Besides, this approach allows obtaining a precise description of the cerebral structures, which is necessary to report data, and also to compute sources of EEG/MEG recordings, as it is often not possible to obtain the MRI of each subject in an infant

population. This atlas should increase the precision of the observed effects for researchers as far as they respect the 10–20 system to locate their recording channels (or know the location of their channels relative to this system).

Cranio-cerebral correlations

In our group of infants, the channels locations of the 10–20 system were rather stable, and consistent with adult studies. Amongst the standard positions, frontal Fp1 and Fp2 were the most stable ones, with the weakest variability, whereas more posterior positions, in particular parietal and occipital points, exhibited larger variability. This may be explained by infant head shape variability due to skull remodelling by sleeping habits or following vaginal birth (e.g. the inion can be particularly difficult to identify on MRI in infants with a flat occiput). This feature is most likely related to the posterior variability in the human head shape, as Okamoto et al. (2004) and Jurcak et al. (2007) reported the same observation in adults.

The location of the channels relative to the template's brain structures can be examined in Fig. 7-A, which reports the channels distribution and variability across infants relative to the template brain. Since the standard locations are examined with respect to the template brain, the description provided here is not fully probabilistic. Still, it provides a first description of the cerebral structures underlying the 10–20 standard locations in a typically developing population of infants with variable head shapes. Fig. 7-B, on the other hand, reports the sulcal distribution and variability across infants relative to the template's 10–20 standard positions. It provides a probabilistic model of the inner cerebral structures in an infant population (9.0 ± 3.6 week-old infants). These two approaches complement each other.

Our results were roughly similar to the locations described by Blume et al. (1974) in post-mortem brains (6 infants younger than 4 months of age and a two-year-old). The differences are likely due to differences in methodology. Infants are lying down in an MRI scanner and were sat to mark the channels location in Blume et al. (1974). Due to its weight, the

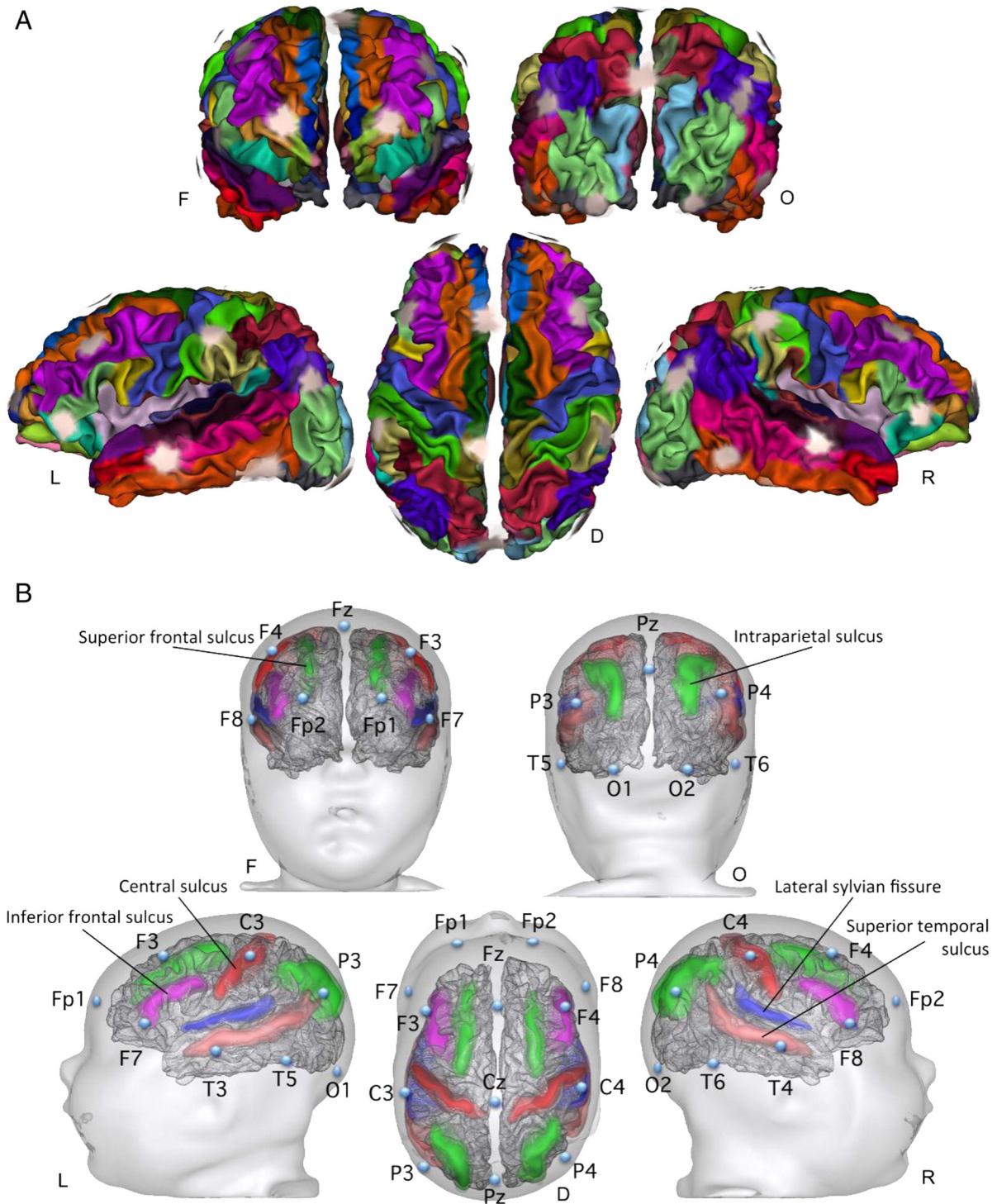


Fig. 7. Cranio-cerebral relationships. A – Projected distributions of the 10–20 standard positions over the anatomically defined brain regions (from left to right and top to down: Frontal – Occipital ; Left – Dorsal – Right views). B – Sulcal presence probability modelled by SPAM, based on 15 infants, and the overlying international 10–20 electrode positions of the template infant (from left to right and top to down: Frontal – Occipital; Left – Dorsal – Right views). Each sulci 3-D representation is modelled by an isosurface corresponding to 60% of the whole probability mass. Note the projection of T5–T6 O1–O2 at the base of the brain, thus lower than the projection reported in adults.

brain might move backward relative to the skull in the scanner but the tight connections at its basis (white matter tracts, sylvian arteries, cerebral falx) might limit its backward movement. By contrast, post-mortem brains are no more inflated by the blood pump and might be packed down by gravity. They also might suffer from oedema due to death-anoxia creating inaccuracies. In any case, the standard locations

along the anterior-posterior axis were similar in both studies whereas the supra-sylvian positions projected somewhat higher along the vertical axis in our study. For instance, we observed that F7–F8 laid at the anterior tip of the inferior frontal sulcus, whilst this pair of locations projected below the frontal lobe in the post-mortem brains. This difference might be due to the sitting position in Blume et al. (1974) or to

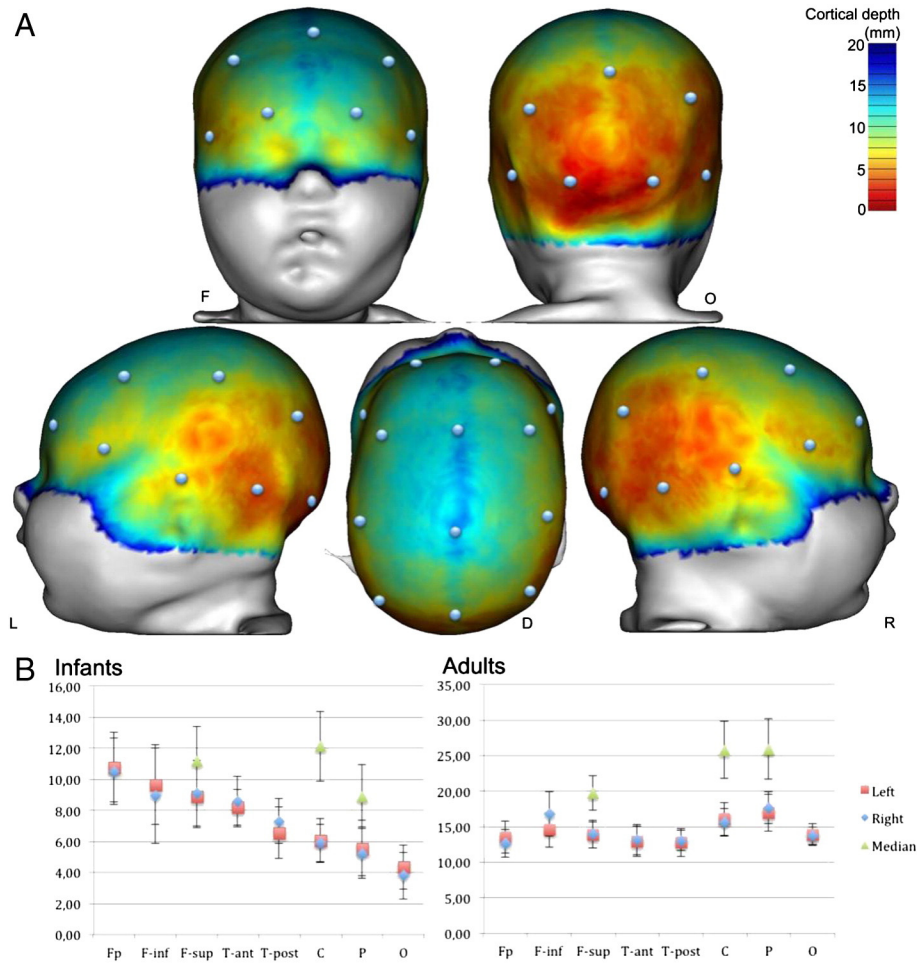


Fig. 8. Cortical depth measurements. A – The mean cortical surface–scalp distances is presented on the template head surface (in millimetres). B – Cortical depth (in millimetres) as a function of electrode location on the skull, for the 16 infant subjects on the left, and as reported by Okamoto et al. (2004) for 17 adult subjects on the right (note the change of scales between the two plots). There is a clear anterior–posterior gradient in infants, but not in adults. At both ages, the most distant channels are those on the midline. No asymmetry is observed for these measures.

the inclusion of preterm infants in their dataset (several infants of this study are described as not having clear frontal sulci which appear at the end of gestation). Indeed, the operculum of the inferior frontal

region, which pushes down the inferior frontal region towards the temporal lobe, only occurs during the last weeks of gestation and first months of post-term life. But the infants' ages are underspecified in this study, so we cannot assess the validity of this hypothesis.

Table 5
Sensors–brain envelope distances and left–right asymmetry measures.

Name	Mean distance (mm)	Standard deviation (mm)	Asymmetry (R vs L)	
			Coefficient	t-test(15) p-value
Fp1	10.75	2.23	–2%	0.63
Fp2	10.48	2.12		
Fz	11.15	2.23		
F3	8.88	2.03	2%	0.50
F4	9.07	2.10		
F7	9.63	2.56	–10%	0.21
F8	8.92	3.05		
Cz	12.12	2.23		
C3	6.03	1.41	–2%	0.72
C4	5.87	1.20		
T3	8.19	1.14	3%	0.43
T4	8.54	1.60		
T5	6.53	1.65	12%	0.09
T6	7.28	1.44		
Pz	8.89	1.99		
P3	5.53	1.77	–6%	0.39
P4	5.17	1.60		
O1	4.35	1.39	–16%	0.16
O2	3.77	1.47		

The main difference between our report in infants and Okamoto et al. (2004) in 17 adults (22–51 years) using MRI is the projection of the lower electrodes (O1–O2, T5–T6). These pairs of electrodes laid just above the inferior limit of the brain (consistent with Blume et al's study in infants), whereas Okamoto and colleagues reported projections over the middle occipital and middle temporal gyri in the adult population. This difference might be related to the globularization of the modern human brain driven by parietal cortex expansion during development (Gunz et al., 2012) or/and by the delayed development of the face (in particularly its lower part), relative to the brain during childhood, which might affect the ear (and thus tragi) positions. By contrast, the anterior temporal location (T3–T4) and the frontal locations projected on similar structures at both ages. For example, C3–C4 were reported over the post-central region in most of the adults, just as in our infant study. This was also the case in Steinmetz et al. (1989) and Towle et al. (1993), but note that two other studies (Homan et al., 1987; Jasper, 1958) located these electrodes over the pre-central region in adults.

Beyond the variability of electrode placement, the location, shape, size of the cortical structures might themselves differ from one subject to the other. Using SPAMs (Perrot et al., 2011), we provided a probabilistic model for the localisation of 6 main sulci (Fig. 7-B). We complemented this localisation information with a measure of dispersion along the

sulci (Fig. 6). The intraparietal sulcus was variable across infants. Indeed, it is often segmented into different subunits by several crossing-folds. The inferior frontal sulcus also exhibited a high dispersion, as it was also shown in adults (Fischl et al., 2008). The sylvian fissure and the superior temporal sulcus, on the contrary, appeared to be the most stable sulci, notably the central region of the sylvian fissure, at the level of Heschl's gyrus, which exhibited a strong consistency between subjects. The enhanced inter-subject variability, at the ends of sulci, is mostly due to differences in sulci lengths.

Electrode-brain distance information

The distance from the scalp to the cortical surface is of crucial importance in NIRS and EEG recordings. We therefore examined inter-subject and inter-channel variations of electrode-brain distances. There was an increase of scalp-brain distances from the occipital to the frontal locations and from the inferior to the superior locations (Fig. 8). Because infants are lying down in the MRI bore, we cannot rule out that the brain weight pushed the CSF forward in lying position but the position of the electrodes along the anterior–posterior axis was similar to Blume et al. (1974) description obtained in sitting infants, and the brain is tightly connected, limiting its movement within the skull. This gradient was not observed in reclining adults (Okamoto et al., 2004) and the scalp-brain distance was rather stable for the different channels at this age (Fig. 8-B). At both ages, the most distant channels were the median channels, because of the superior sagittal sinus running in the inter-hemispheric region.

Researchers must thus be aware that their sensors might be more or less distant from the brain. Sensor-brain distances, which affect signal amplitude, can vary by a factor of 3 between locations (4–12 mm). Furthermore, distances between important landmarks and their closer scalp electrodes were often superior to 20 mm, and for some landmarks close to 30 mm (e.g. Cz to the hand knob). Odabae et al. (2013) showed that the EEG amplitude in neonates decays rapidly and reached the noise level at around 50 mm from the amplitude peak for the 12–20 Hz frequency band. Although for slower latencies, the decline was less steep, this study confirms modelling scalp EEG as a more focal signal than in adults because of the higher medium conductivity in infants (Grieve et al., 2003, 2004). It is noteworthy to signal that Odabae et al.'s observation of a steeper voltage decay slope over parietal areas than over inter-hemispheric fissure is probably due to the increased electrode-brain distance over the midline.

The inter-subject variability may seem small (3–8 mm, 5 mm in average, for the distances reported in Table 6) but given the amplitude decreasing slope described in Odabae et al. (2013), it represents a 10% variability in the amplitude between subjects. A high-density coverage of the head is thus crucial for a correct spatial sampling of the EEG activity in infants as already advocated in Grieve et al. (2003, 2004) and Odabae et al. (2013).

Distance to the internal structures is also at stake for NIRS measurements as the measure is done in the crescent of light between the light emitter and the detector. The diode spacing commonly used in infants is sufficient to reach the brain. For example, a spacing of 20 mm between source and detector allowed reaching a depth of 10 mm with the same iso-sensitivity (Patil et al., 2011). However, NIRS experimenters should avoid midline locations and move the sensors above the region of interest as the 10–20 classical locations might be too far from critical brain structures. It might be useful to increase the source-detector distances above 20 mm if the goal is to record from frontal areas and anterior temporal areas (Fig. 8) at the expense of a decrease in signal intensity.

Left–right asymmetries

Anatomical asymmetries are observed from the preterm period on (Chi et al., 1977; Dubois et al., 2008, 2010; Glasel et al., 2011; Habas et al., 2012; Sowell et al., 2002; Toga and Thompson, 2003) and several maturational markers indicate a different developmental time-course of the left and right human hemispheres (Chiron et al., 1997; Dubois et al., 2009; Leroy et al., 2011a; Lin et al., 2012). To study functional asymmetries, it is thus necessary to control for the known structural asymmetries which can affect channel/brain structures relations.

Beauchamp et al. (2011) recently reported significant left–right asymmetries in brain-scalp distances measured from T1w images in 0–18 month-old infants, at different cortical landmarks. In line with this idea, we performed brain-scalp measurements for each of the 10–20 standard positions, and found no asymmetry at these points. Note however, that we actually computed distances between the brain envelope and the scalp; we might therefore have occulted some anatomical asymmetries in the depth of the sulci but this is also the case in Beauchamp et al. (2011) where the authors chose external brain landmarks (i.e. not in the depth of sulci). We also computed distances between some remarkable cortical structures and the closest 10–20 standard positions. In particular, for the lateral edge of the Heschl's sulcus, we found neither asymmetry in distances to standard positions

Table 6
Distance from four cortical landmarks to closest international 10–20 standard positions (and tragus), and left–right asymmetry measures.

Structure	Electrodes	Mean distance (mm)	SD (mm)	Asymmetry (R vs L)	
				Coefficient	t-test (15) p-value
Hand knob	Left-Cz	34.77	2.97	1%	0.76
	Right-Cz	35.36	4.54		
	Left-C3	23.80	3.87		
	Right-C4	22.60	4.23		
Ventre-lateral end of the pars triangularis	Left-F3	30.10	6.87	4%	0.49
	Right-F4	30.86	3.59		
	Left-F7	20.71	4.53		
	Right-F8	19.90	3.39		
Lateral edge of Heschl's sulcus	Left-T3	20.13	4.62	–8%	0.34
	Right-T4	18.60	4.59		
	Left-T5	35.87	5.25		
	Right-T6	35.79	4.85		
Posterior end of the sylvian fissure	Left-C3	22.32	6.20	–27%	0.07
	Right-C4	17.01	5.73		
	Left-P3	25.95	5.19		
	Right-P4	31.98	5.94		
	Left-Tragus	72.01	6.40		
	Right-Tragus	71.89	8.30		

T3–T4 nor T5–T6, whilst [Beauchamp et al. \(2011\)](#) reported a strong asymmetry for distances to the skull. Similarly, we did not find asymmetry when measuring the distance from the tragus to the posterior end of sylvian fissure, replicating [Mahmoudzadeh et al. \(2013\)](#) in preterm infants. Authors JD and GDL were present during data acquisition and were attentive to a symmetrical placement of the infant head in the coil to reduce CSF accumulation on one side, for preventing left–right differences in subsequent post-processing steps. A correct placement in the coil is more difficult to ensure when data are coming from database and may partially explain the difference between these two sets of data (see for example Fig. 2 in [Beauchamp et al., 2011](#), in which the presented axial image is tilted to the left of the image).

We observed only one significant distance asymmetry for the posterior end of the sylvian fissure ($p = .016$, [Table 6](#)), due to the known difference in the slopes of the left and right sylvian fissure (the right fissure is shorter, steeper and more dorsal than the left from the preterm period on). P3 and P4 (and also C3–C4) were not at the same distance from the posterior end of the sylvian fissure. Thus, sensors were at the same distance from the brain envelope on the left and right sides, but the best location to record from homologous posterior peri-sylvian structures might be slightly different on the right and left sides. This should be taken into account when functional asymmetries are discussed.

Conclusion

In this study, we presented an infant brain atlas based on a single subject (7.1 week-old girl), complemented with a probabilistic description of the 10–20 standard positions with respect to the underlying brain structures, and a probabilistic model of the sulcal folding patterns. The template and all maps provided in this article can be downloaded (<http://www.unicog.org/pm/pmwiki.php/Site/InfantTemplate>). We hope that this work will help the community converge to a unified analysis framework for infant brain recordings. Still, further studies are needed in order to cover the various stages of brain development, and to grow the body of knowledge in the field of neonatal/paediatric neuroimaging.

Acknowledgments

This research was supported by La Fondation Motrice, la Fondation de France, la Fondation Bettancourt, la Fondation Fyssen, l'Ecole des Neurosciences de Paris and the McDonnell foundation. The finalisation of this work received support from the European Union Seventh Framework Programme (FP7/2007–2013, grant agreement no. 604102). We are particularly grateful to Neurospin staff for their daily help and at last but not least we thank infants and parents for their participation. We thank the two anonymous reviewers for their thorough reading and to have raised discussion points about the EEG focal responses in infants.

References

Akiyama, L.F., Richards, T.R., Imada, T., Dager, S.R., Wroblewski, L., Kuhl, P.K., 2013. Age-specific average head template for typically developing 6-month-old infants. *PLoS ONE* 8 (9), e73821.

Altaye, M., Holland, S.K., Wilke, M., Gaser, C., 2008. Infant brain probability templates for MRI segmentation and normalization. *NeuroImage* 43 (4), 721–730.

Barkovich, A.J., 2000. Concepts of myelin and myelination in neuroradiology. *AJNR Am. J. Neuroradiol.* 21 (6), 1099–1109.

Beauchamp, M.S., Beurlot, M.R., Fava, E., Nath, A.R., Parikh, N.A., Saad, Z.S., et al., 2011. The developmental trajectory of brain–scalp distance from birth through childhood: implications for functional neuroimaging. *PLoS ONE* 6 (9), e24981.

Blume, W.T., Buza, R.C., Okazaki, H., 1974. Anatomic correlates of the ten–twenty electrode placement system in infants. *Electroencephalogr. Clin. Neurophysiol.* 36, 303–307.

Chi, J.G., Dooling, E.C., Gilles, F.H., 1977. Gyral development of the human brain. *Ann. Neurol.* 1, 86–93.

Chiron, C., Jambaque, I., Nabbut, R., Lounes, R., Szyrota, A., Dulac, O., 1997. The right brain hemisphere is dominant in human infants. *Brain* 120, 1057–1065.

Cointepas, Y., Mangin, J.F., Garnero, L., Poline, J.B., Benali, H., 2001. BrainVISA: software platform for analysis of multi-modality brain data. *NeuroImage* 13 (6), S98.

Dehaene-Lambertz, G., Dehaene, S., Hertz-Pannier, L., 2002. Functional neuroimaging of speech perception in infants. *Science* 298 (5600), 2013–2015.

Dubois, J., Benders, M., Cachia, A., Lazeyras, F., Ha-Vinh Leuchter, R., Sizonenko, S.V., et al., 2008. Mapping the early cortical folding process in the preterm newborn brain. *Cereb. Cortex* 18 (6), 1444–1454.

Dubois, J., Hertz-Pannier, L., Cachia, A., Mangin, J.F., Le Bihan, D., Dehaene-Lambertz, G., 2009. Structural asymmetries in the infant language and sensori-motor networks. *Cereb. Cortex* 19 (2), 414–423.

Dubois, J., Benders, M., Lazeyras, F., Borradori-Tolsa, C., Leuchter, R.H., Mangin, J.F., et al., 2010. Structural asymmetries of perisylvian regions in the preterm newborn. *NeuroImage* 52 (1), 32–42.

Evans, A., Collins, D., Neelin, P., MacDonald, D., Kamber, M., Marrett, T., 1994. Three-dimensional correlative imaging: applications in human brain mapping. *Funct. Neuroimaging* 145–162.

Fonov, V., Evans, A.C., Botteron, K., Almli, C.R., McKinstry, R.C., Collins, D.L., 2011. Unbiased average age-appropriate atlases for pediatric studies. *NeuroImage* 54 (1), 313–327.

Gilmore, J.H., Lin, W., Prastawa, M.W., Looney, C.B., Vetsa, Y.S., Knickmeyer, R.C., et al., 2007. Regional gray matter growth, sexual dimorphism, and cerebral asymmetry in the neonatal brain. *J. Neurosci.* 27 (6), 1255–1260.

Glaser, H., Leroy, F., Dubois, J., Hertz-Pannier, L., Mangin, J.F., Dehaene-Lambertz, G., 2011. A robust cerebral asymmetry in the infant brain: the rightward superior temporal sulcus. *NeuroImage* 58, 716–723.

Grieve, P.G., Emerson, R.G., Fifer, W.P., Isler, J.R., Stark, R.L., 2003. Spatial correlation of the infant and adult electroencephalogram. *Clin. Neurophysiol.* 114 (9), 1594–1608.

Grieve, P.G., Emerson, R.G., Isler, J.R., Stark, R.L., 2004. Quantitative analysis of spatial sampling error in the infant and adult electroencephalogram. *NeuroImage* 21 (4), 1260–1274.

Gunz, P., Neubauer, S., Golovanova, L., Doronichev, V., Maureille, B., Hublin, J.-J., 2012. A uniquely modern human pattern of endocranial development. Insights from a new cranial reconstruction of the Neandertal newborn from Mezmaiskaya. *J. Hum. Evol.* 62 (2), 300–313.

Habas, P.A., Scott, J.A., Roosta, A., Rajagopalan, V., Kim, K., Rousseau, F., et al., 2012. Early folding patterns and asymmetries of the normal human brain detected from in utero MRI. *Cereb. Cortex* 22 (1), 13–25.

Hellstöm, B., Karlsson, B., Müssbichler, H., 1963. Electrode placement in EEG of infants and its anatomical relationship studied radiographically. *Electroencephalogr. Clin. Neurophysiol.* 15 (1), 115–117.

Homan, R.W., Herman, J., Purdy, P., 1987. Cerebral location of international 10–20 system electrode placement. *Electroencephalogr. Clin. Neurophysiol.* 66 (4), 376–382.

Jasper, H.H., 1958. The ten twenty electrode system of the international federation. *Electroencephalogr. Clin. Neurophysiol.* 10, 371–375.

Jurcak, V., Tsuzuki, D., Dan, I., 2007. 10/20, 10/10, and 10/5 systems revisited: their validity as relative head-surface-based positioning systems. *NeuroImage* 34 (4), 1600–1611.

Kuklisova-Murgasova, M., Aljabar, P., Srinivasan, L., Counsell, S.J., Doria, V., Serag, A., et al., 2011. A dynamic 4D probabilistic atlas of the developing brain. *NeuroImage* 54 (4), 2750–2763.

Le Troter, A., Auzias, G., Coulon, O., 2012. Automatic sulcal line extraction on cortical surfaces using geodesic path density maps. *NeuroImage* 61 (4), 941–949.

Leroy, F., Glaser, H., Dubois, J., Hertz-Pannier, L., Thirion, B., Mangin, J.F., et al., 2011a. Early maturation of the linguistic dorsal pathway in human infants. *J. Neurosci.* 31 (4), 1500–1506.

Leroy, F., Mangin, J.F., Rousseau, F., Glaser, H., Hertz-Pannier, L., Dubois, J., et al., 2011b. Atlas-free surface reconstruction of the cortical grey-white interface in infants. *PLoS ONE* 6 (11), e27128.

Lin, P.-Y., Roche-Labarbe, N., Dehaes, M., Fenoglio, A., Grant, P.E., Franceschini, M.A., 2012. Regional and hemispheric asymmetries of cerebral hemodynamic and oxygen metabolism in newborns. *Cereb. Cortex* 23, 339–348.

Mahmoudzadeh, M., Dehaene-Lambertz, G., Fournier, M., Kongolo, G., Gadjil, S., Dubois, J., et al., 2013. Syllabic discrimination in premature human infants prior to complete formation of cortical layers. *PNAS* 110, 4846–4851.

Matsui, M., Homae, F., Tsuzuki, D., Watanabe, H., Katagiri, M., Uda, S., et al., 2014. Referential framework for transcranial anatomical correspondence for fNIRS based on manually traced sulci and gyri of an infant brain. *Neurosci. Res.* 80, 55–68.

Odabae, M., Freeman, W.J., Colditz, P.B., Ramon, C., Vanhatalo, S., 2013. Spatial patterning of the neonatal EEG suggests a need for a high number of electrodes. *NeuroImage* 68, 229–235.

Okamoto, M., Dan, H., Sakamoto, K., Takeo, K., Shimizu, K., Kohno, S., et al., 2004. Three-dimensional probabilistic anatomical cranio-cerebral correlation via the international 10–20 system oriented for transcranial functional brain mapping. *NeuroImage* 21 (1), 99–111.

Patil, A.V., Safaie, J., Moghaddam, H.A., Wallois, F., Grebe, R., 2011. Experimental investigation of NIRS spatial sensitivity. *Biomed. Opt. Expr.* 2 (6), 1478–1493.

Perrot, M., Rivière, D., Mangin, J.-F., 2011. Cortical sulci recognition and spatial normalization. *Med. Image Anal.* 15 (4), 529–550.

Riviere, D., Papadopoulos, D., Poupon, C., Poupon, F., Coulon, O., Poline, J.-B., et al., 2000. A structural browser for human brain mapping. *NeuroImage* 11 (5, Supplement), S912.

Sowell, E.R., Thompson, P.M., Rex, D., Kornsand, D., Tessner, K.D., Jernigan, T.L., et al., 2002. Mapping sulcal pattern asymmetry and local cortical surface gray matter distribution in vivo: maturation in perisylvian cortices. *Cereb. Cortex* 12 (1), 17–26.

Steinmetz, H., Fürst, G., Meyer, B.-U., 1989. Craniocerebral topography within the international 10–20 system. *Electroencephalogr. Clin. Neurophysiol.* 72 (6), 499–506.

Tadel, F., Baillet, S., Mosher, J.C., Pantazis, D., et al., 2011. Brainstorm: a user-friendly application for MEG/EEG analysis. *J. Comput. Intell. Neurosci.* 2011, 13.

Talairach, J., Tournoux, P., 1988. *Co-Planar Stereotaxic Atlas of the Human Brain. 3-Dimensional Proportional System: An Approach to Cerebral Imaging*. Translated

- by Mark Rayport Thieme Medical Publishers Inc., New York, (Stuttgart New York: George Thieme Verlag).
- Toga, A.W., Thompson, P.M., 2003. Mapping brain asymmetry. *Nat. Rev. Neurosci.* 4 (1), 37–48.
- Towle, V.L., Bolaños, J., Suarez, D., Tan, K., Grzeszczuk, R., Levin, D.N., et al., 1993. The spatial location of EEG electrodes: locating the best-fitting sphere relative to cortical anatomy. *Electroencephalogr. Clin. Neurophysiol.* 86 (1), 1–6.
- Tsuzuki, D., Dan, I., 2013. Spatial registration for functional near-infrared spectroscopy: from channel position on the scalp to cortical location in individual and group analyses. *NeuroImage* 85, 92–103.
- Tzourio-Mazoyer, N., Landeau, B., Papathanassiou, D., Crivello, F., Etard, O., Delcroix, N., et al., 2002. Automated anatomical labeling of activations in SPM using a macroscopic anatomical parcellation of the MNI MRI single-subject brain. *NeuroImage* 15 (1), 273–289.